

# Inverse Design of Metasurface based Absorbers using Physics Guided Conditional Diffusion Models

Vineetha Joy<sup>1\*</sup>, Jamshed Palai<sup>1</sup>, Satwik Sahoo<sup>2</sup>, Anshuman Kumar<sup>3</sup>, Amit Sethi<sup>3</sup>, Hema Singh<sup>1</sup>

<sup>1</sup>Centre for Electromagnetics, CSIR-National Aerospace Laboratories, Kodihalli, Bangalore 560017

<sup>2</sup>Birla Institute of Technology and Science, Pilani, Rajasthan 333031

<sup>3</sup>Indian Institute of Technology, Bombay, Maharashtra 400076

vineethajoy@nal.res.in, ompalai11@gmail.com; stwk17@gmail.com; anshuman.kumar@iitb.ac.in, asetithi@iitb.ac.in, hemasingh@nal.res.in

**Abstract**— Inverse design of metasurfaces for specific electromagnetic responses requires generating geometries that satisfy stringent spectral constraints while maintaining manufacturability. Conventional design methodologies rely on iterative optimization routines using full-wave simulations, which become extremely time-consuming and computationally intensive for large design spaces. In addition, commonly employed generative approaches often exhibit limited conditional fidelity and the generated designs often contain fine or irregular features that are impractical to fabricate. In this regard, we propose a physics guided condition-quality enhanced diffusion framework for the inverse design of metasurface based absorbers. Here, the conditioning information consisting of target reflection characteristics is integrated into the model using feature-wise linear modulation (FiLM). FiLM mechanism significantly improves conditional alignment and spectral controllability across the diffusion denoising process. Furthermore, to enforce adherence to target spectra, a pre-trained surrogate EM simulator is embedded into the framework introducing physics-aware regularization through spectrum-level loss functions. The efficiency of the proposed model is demonstrated by generating practically realizable metasurfaces for different types of reflection characteristics in the frequency range of 2–18 GHz. The proposed framework achieves an average spectral mean squared error of 0.0006 and band alignment accuracy of 0.958 between the target spectra and the spectra produced by the generated designs, demonstrating high conditional accuracy. In addition, the model generates multiple geometrically distinct patterns for the same condition, thereby providing diverse design alternatives to the engineer. The proposed model produces the suitable design in approximately 30 seconds, whereas the conventional approach can take several months under comparable computational resources. The efficiency of the model is also established via experimental measurements.

**Keywords**—Metasurfaces, Absorbers, Diffusion models, feature-wise linear modulation (FiLM), Conditioning Quality.

## I. INTRODUCTION

Metasurfaces are two-dimensional, artificially engineered structures composed of subwavelength scatterers called meta atoms [1]. By tailoring the geometry, constituent materials, and spatial arrangement of these meta atoms, metasurfaces can precisely manipulate the amplitude, polarization, and phase of incident electromagnetic (EM) waves. If a metasurface with sub-wavelength resonators is placed at the boundary between two homogeneous media, the reflection and transmission characteristics will alter as per generalized Snell's laws of refraction and reflection [2], [3]. This happens because the metasurface induces a resonant response that modifies the phase of the wave. Hence, the direction and characteristics of the incident wavefront can be modified by varying the

geometry and spatial arrangement of meta atoms on a metasurface. Further, from the perspective of practical realization, metasurfaces can be easily fabricated and are more space efficient than their three-dimensional counterparts, i.e. metamaterials. These attractive attributes have made metasurfaces highly promising for applications such as stealth technology [4]-[6], invisibility cloaking [7], electromagnetic shielding [8], holographic imaging [9], [10], wireless communication [11], [12], lensing [13], [14], optical multiplexing [15] etc.

The inverse design of metasurfaces (Fig. 1) where specific EM responses must be mapped to physical structures is a very challenging task. This is due to the high dimensionality, nonlinearity, and non-uniqueness inherent in the design space. Conventional design approaches typically rely on the intuition of the designer, rigorous parametric sweeps, and iterative full-wave simulations to arrive upon a suitable design [16]-[19]. While effective for simple configurations, these methods become excessively time-consuming and computationally intensive for metasurfaces with even moderate design complexity. This process often requires hundreds or thousands of EM simulations each of which can take minutes to hours. Various optimization-based methods [20] such as topology optimization [21], [22], genetic algorithms [23]-[26], ant-colony optimization [27]-[29], particle swarm optimization (PSO) [30], [31], etc. have been developed to improve the efficiency of the above-mentioned traditional design scheme. These algorithms rely on iteratively evaluating the performance of candidate structures until a specific criterion is met. Although these approaches outperform manual trial-and-error strategies, they are still constrained by slow convergence requiring large number of iterations, high computational cost due to repeated full-wave simulations, susceptibility to local optima, and limited generalizability. Moreover, they often require complete re-optimization for each new performance specification, making them impractical for multi-objective design tasks involving broadband or multi-band responses.

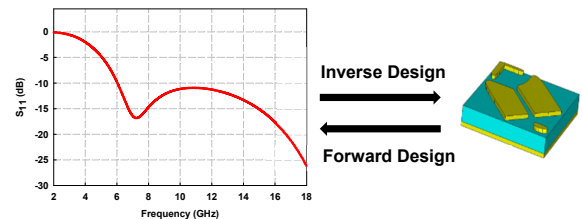


Fig. 1. Illustration of forward and inverse design of metasurface based absorbers

To overcome the limitations of traditional approaches, deep learning (DL) has emerged as a powerful alternative

for inverse design of metasurfaces [32], [33]. DL techniques can efficiently explore high-dimensional design spaces and rapidly generate meta atom configurations that satisfy specific EM performance criteria. Once trained, DL models offer near-instantaneous predictions, eliminating the need for iterative full-wave simulations for every new design target. Initial approaches focused on predicting the structural parameters of predefined geometries by training on datasets composed of explicit input–output pairs, where each design parameter set is linked to its corresponding EM response. Through iterative training, the network learns to infer suitable parameter combinations that achieve specific EM responses [34]-[36]. Several models adopted a tandem architecture, coupling an inverse neural network with a forward network to address the intrinsic non-uniqueness of the inverse problem and ensure physical consistency between predicted geometries and EM responses [37]-[39]. However, these early methods have serious limitations, especially for the design of free-form shapes, where high randomness and weak symmetry make it hard for standard networks to generalize well.

Extending beyond conventional DL approaches, generative models enable the generation of novel structures by learning and sampling from the underlying distributions of complex, high-dimensional datasets. Generative adversarial networks (GANs), particularly their conditional variants (cGANs), enable the generation of complex, free-form geometries conditioned on target EM responses [40]-[45]. To address typical GAN training problems such as mode collapse and unstable convergence, researchers have also adopted the Wasserstein GAN with gradient penalty (WGAN-GP), which provides more stable training and helps maintain diversity in the generated metasurface designs [46]-[48]. Autoencoders offer an alternative generative framework for inverse design of metasurfaces by constructing latent spaces that enable design exploration [49]. Variational autoencoders (VAE) have been used to embed metasurface structures and their scattering responses into a low-dimensional latent space, where PSO has been applied to identify optimal latent variables and consequently the corresponding metasurface structure [50]-[52]. They have also been successfully applied to realize various metasurface functionalities, including absorber designs [53]-[55] and for generating user specific structural color [56]. Recent hybrid approaches even combined VAEs with quantum GANs for enhanced optimization [57].

However, it is to be noted that, GANs and VAEs face significant limitations in inverse design applications. Traditional VAEs suffer from characteristic limitations including blurred reconstructions due to the reconstruction loss balanced against KL divergence, limited diversity and the requirement for additional optimization algorithms in latent space adding further computational overhead to the design workflow. GANs, while capable of generating high-quality structures, suffer from fundamental instability caused by the adversarial training process, making consistent conditioning on performance requirements difficult. Although cGANs were developed to address conditioning challenges, they were restricted to categorical conditions. Hence, they do not perform well in engineering applications where conditions are performance metrics which are continuous variables. Although continuous

conditional GANs were introduced to address continuous conditioning, their success has largely been confined to computer vision applications [58] and they have been designed to condition generation on scalar performance metrics [59]. Diffusion-based generative models have recently emerged as promising tools due to their ability to learn the progressive noise corruption process and recover high-quality samples through iterative denoising. These models have demonstrated superior generation quality and accuracy compared to GAN and VAE-based approaches across several application domains, including text-to-image synthesis, image super-resolution, and metasurfaces [60]-[61].

In this regard, the present paper proposes a condition-quality enhanced diffusion framework for the inverse design of metasurface based radar absorbing structures (RAS). Here, the conditioning information consisting of target reflection characteristics and material properties is integrated into the model using feature-wise linear modulation (FiLM). FiLM mechanism significantly improves conditional alignment and spectral controllability across the diffusion denoising process. Furthermore, a pre-trained surrogate EM simulator (SES) is integrated into the framework to evaluate how closely the generated designs satisfy the user-specified conditions. Incorporating this assessment directly into the loss function helps to maintain high conditioning accuracy during generation.

The proposed diffusion-based framework takes frequency-dependent reflection characteristics together with material properties as inputs to the model. Incorporating material properties as part of the input, rather than predicting them at the output, ensures that the generated designs remain physically realizable using commercially available materials and feasible thicknesses. Further, in contrast to most existing approaches that generate only the meta-atom geometry while keeping design factors such as pattern material fixed, the proposed model simultaneously predicts the complete metasurface configuration, including the pattern material and its corresponding resistivity. The model has been trained on a custom built dataset comprising 30 classes of meta atom geometries, enabling the synthesis of a wide variety of EM spectra. Furthermore, to address dataset imbalance, where certain spectral characteristics dominate and bias the learning process, a thorough data analysis and selective data augmentation has been carried out. Following this, a weighted sampling-based training strategy has been employed. This ensures uniform learning across different spectral categories and improves the robustness of the model in capturing diverse metasurface responses. The performance of the model has been assessed using several examples across the broad frequency range of 2GHz – 18GHz. To demonstrate the practical realizability of the metasurface configurations generated by the proposed model, a planar RAS based on the generated meta-atom has been fabricated and experimentally measured. The measured spectra, simulated and target spectra have been compared as well.

This paper is organized as follows. Section II presents the theoretical background of the loss functions employed in the proposed model. The overall architecture of the framework is described in Section III, followed by a

detailed discussion of the training dataset in Section IV. Section V demonstrates the capabilities of the proposed approach through representative design examples. Section VI presents the results of ablation analysis followed by Section VII presenting details of experimental measurements and validation. Finally, conclusions are drawn in Section VIII.

## II. THEORETICAL BACKGROUND

Diffusion models are generative frameworks based on two complementary stages (Fig. 2): a forward diffusion process ( $q$ ) and a reverse denoising process ( $p$ ) [62]. In the forward stage, the 3-channel image representing the original meta-atom is progressively corrupted by adding noise. The model is then trained to learn the reverse of this process, enabling it to reconstruct the original meta-atom from its noisy representation.

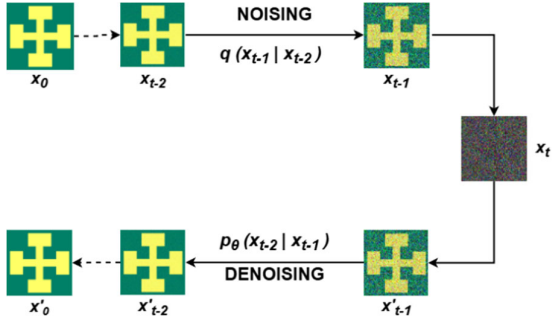


Fig. 2. Forward and backward processes in a diffusion model.

The forward process ( $q$ ) gradually adds noise to the original image  $x_0$  in  $T$  steps following a predefined variance schedule  $\beta_1, \beta_2, \dots, \beta_T$  as given below [64]:

$$q(x_t | x_{t-1}) = N(x_t; \sqrt{(1-\beta_t)} \cdot x_{t-1}, \beta_t \cdot I) \quad (1)$$

$$q(x_{1:T} | x_0) = \prod_{t=1}^T q(x_t | x_{t-1}) \quad (2)$$

The variance parameter  $\beta_t$  increases with each timestep ( $t$ ), resulting in progressively higher levels of noise being added to the image. Through this iterative noise injection process, the meta-atom representation gradually converges toward a Gaussian distribution.

By applying a re-parameterization technique, the corrupted image of meta-atom ( $x_t$ ) at any arbitrary time step  $t$  can be expressed directly in terms of the original image  $x_0$  through a closed-form relationship as given below:

$$x_t = \sqrt{\bar{\alpha}_t} x_0 + \varepsilon \sqrt{1 - \bar{\alpha}_t}, \text{ where } \varepsilon \sim N(0,1) \quad (3)$$

Where,  $\alpha_t = 1 - \beta_t$  and  $\bar{\alpha}_t = \prod_{s=1}^t \alpha_s$

The reverse denoising process ( $p$ ) constitutes the core generative mechanism wherein the model learns to systematically remove noise and reconstruct the original data distribution. It can be represented as,

$$p_\theta(x_{t-1} | x_t) = N(x_{t-1}; \mu_\theta(x_t, t), \Sigma_\theta(x_t, t)) \quad (4)$$

During training,  $p_\theta(x_{t-1} | x_t)$  should become as close as possible to  $q(x_{t-1} | x_t)$ . This can be enforced by optimizing the variational lower bound ( $L$ ) on negative log likelihood as given below,

$$E[-\log p_\theta(x_0)] \leq E_q \left[ -\log \left( \frac{p_\theta(x_{0:T})}{q(x_{1:T} | x_0)} \right) \right] = L \quad (5)$$

$$L \propto \sum_{t>1} D_{KL}(q(x_{t-1} | x_t, x_0) \| p_\theta(x_{t-1} | x_t)) \quad (6)$$

Hence, the problem transforms into minimizing the Kullback–Leibler divergence ( $D_{KL}$ ) between the true distribution ( $q(x_{t-1} | x_t)$ ) and the distribution characterized by the neural network ( $p_\theta(x_{t-1} | x_t)$ ). This problem is equivalent to training a neural network  $\varepsilon_\theta(x_t, t)$  to predict the noise  $\varepsilon$  that was added at each time step during the forward process, i.e.

$$\min_\theta L(\theta) = E_{\{x_0, \varepsilon, t\}} \left[ \|\varepsilon_t - \varepsilon_\theta(x_t, t)\|^2 \right] \quad (7)$$

where  $\theta$  represents the model parameters, and  $x_t$  can be obtained from (3).

Further, in order to steer the generation of meta atom geometries towards a specific condition  $c$ , i.e., reflection characteristics along with material properties, a guidance mechanism is required. In the present work, classifier-free guidance (CFG) is employed to achieve conditional generation by jointly training the model on both conditional and unconditional objectives [63]. The neural network  $\varepsilon_\theta$  is now conditioned on  $c$ , denoted as  $\varepsilon_\theta(x_t, t, c)$ . During training, the model is presented with the conditioning vector  $c$  for most of the training steps. However, for a fixed percentage of steps,  $c$  is replaced with a null token  $\phi$ , forcing the model to learn the unconditional generation path as well. During inference, the model makes two predictions at each time step  $t$ : conditional noise prediction  $\varepsilon_\theta(x_t, t, c)$  and unconditional noise prediction  $\varepsilon_\theta(x_t, t, \phi)$ . The final predicted noise  $\hat{\varepsilon}_\theta$  is then computed as:

$$\hat{\varepsilon}_\theta(x_t, t, c) = \varepsilon_\theta(x_t, t, c) + w(\varepsilon_\theta(x_t, t, c) - \varepsilon_\theta(x_t, t, \phi)) \quad (8)$$

Where  $w$  is the guidance scale that controls the extent of conditioning. The training objective remains the same as in equation (7), but is now applied to the conditional model. The guided noise prediction  $\hat{\varepsilon}_\theta$  calculated in equation (8) is used in place of  $\varepsilon_\theta$  in equation (7) to generate the sample for the previous timestep,  $x_{t-1}$ .

To improve conditional fidelity in the diffusion process, FiLM is employed in this work to incorporate conditioning information into the denoising network [64]. FiLM enables feature-wise modulation of intermediate activations based on input condition  $c$ , allowing the model to adapt its internal representations according to the desired EM specifications while maintaining architectural simplicity. Unlike concatenation-based conditioning, FiLM directly modifies feature activations, enabling efficient propagation of conditioning information across the network. Let  $F$  denote the feature map from a particular layer in the network and  $c$  denote the condition. FiLM modulates the feature map using a learned affine transformation as given below:

$$FiLM(F) = \gamma(c)F + \beta(c) \quad (9)$$

Where  $\gamma(c)$  and  $\beta(c)$  are learned functions of  $c$ . A FiLM layer is illustrated in Fig. 3b.

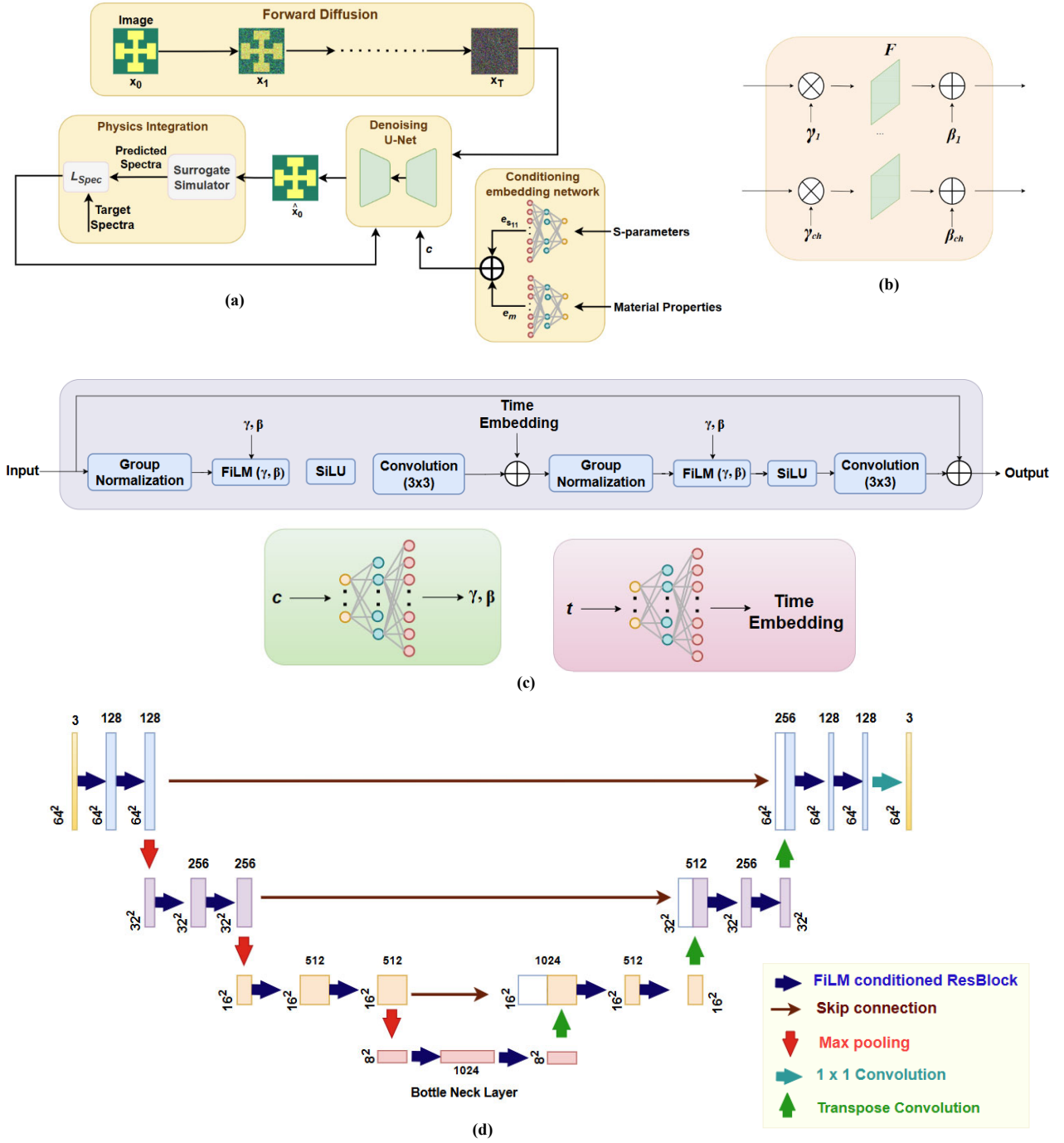


Fig. 3. Architecture of the proposed inverse design framework (a) Complete block diagram (b) A FiLM layer ( $ch$  denotes the number of channels in the feature map) (c) FiLM conditioned ResBlock (d) Denoising U-Net.

Further, in order to incorporate physics into the generative framework, a pre-trained surrogate EM simulator (SES) is plugged into the diffusion model to map the generated metasurface geometry to its corresponding reflection characteristics. For a generated sample  $x_0$ , the surrogate model predicts the spectrum ( $S_{11(gen)}$ ), which is then compared with the target spectrum ( $S_{11(target)}$ ). A spectral consistency loss ( $L_{spec}$ ) is defined as the mean squared error between the predicted and the target spectra,

$$L_{spec} = \sum_{i=1}^{N_f} \left( \left| S_{11(gen)}(f_i) \right| - \left| S_{11(target)}(f_i) \right| \right)^2 \quad (10)$$

Where  $N_f$  refer to the number of frequency ( $f$ ) points. This loss enforces physical consistency by penalizing deviations of the generated designs from the desired EM response.

The overall loss function of the proposed inverse design framework has been then formulated as given below:

$$L = w_R L_R + w_G L_G + w_B L_B + \lambda L_{spec} \quad (11)$$

Where  $L_R$ ,  $L_G$  and  $L_B$  denote the diffusion loss as given in equation (7) computed across the three channels of the generated image of meta-atom.  $w_R$ ,  $w_G$ ,  $w_B$  and  $\lambda$  are hyper parameters controlling the influence of different loss components during training.

### III. ARCHITECTURE OF THE NETWORK

The architecture of the proposed framework, as shown in Fig. 3, is designed to generate 3-channel colored images representing metasurface configurations that satisfy specified reflection characteristics using a particular substrate material. The main components of the proposed framework are described below:

(i) *Condition embedding network*: To incorporate the conditioning information into the generative process, a dedicated condition embedding network is employed. The conditioning input consists of the target reflection spectrum  $S_{11}$  and the corresponding material parameters. Since these inputs represent different physical attributes, they are processed through separate embedding networks to extract meaningful feature representations. The resulting embeddings are then concatenated to form a unified condition vector,  $c=[e_{S_{11}}, e_m]$

where  $e_{S_{11}}$  and  $e_m$  denote the spectral and material embeddings, respectively. This combined embedding serves as the conditioning input to the diffusion model.

(ii) *Conditional diffusion-based generative network*: The diffusion model serves as the generative backbone of the proposed framework and it follows the standard diffusion paradigm as described in Section II. During training, the forward diffusion process progressively corrupts the original metasurface image by adding Gaussian noise across multiple timesteps. The reverse diffusion process is implemented using a U-Net based denoising architecture with an encoder-decoder structure and residual convolutional blocks. The encoder extracts hierarchical spatial features from the noisy input, while the decoder reconstructs the metasurface geometry through successive up sampling operations. Skip connections preserve fine spatial details and enable accurate reconstruction of geometric patterns. During training, the network receives the noisy image, diffusion time step and condition and learns to predict the noise component, thereby recovering the clean geometry. To strengthen conditional control, classifier-free guidance is adopted as mentioned in Section II. During inference, generation begins from random Gaussian noise, and the trained denoising network iteratively removes noise through the reverse diffusion process to produce a metasurface design satisfying the conditioning constraints.

(iii) *Conditioning via FiLM Modulation*: To guide the generation process towards the desired EM response, FiLM based conditioning is incorporated within the residual blocks of the denoising U-Net as shown in Fig. 3c. A multi-layer perceptron neural network (MLP) processes the condition vector (c) and generates the modulation parameters ( $\gamma$ ,  $\beta$ ) that are injected into multiple layers of the denoising network. These parameters modulate

intermediate feature maps through feature-wise scaling and shifting operations thus enabling the conditioning information to influence the feature representations across the entire network.

(iv) *Surrogate-based physics integration*: To enforce EM constraints in the generated designs, a pre-trained surrogate model is integrated into the training pipeline. During training, the metasurface geometry generated by the diffusion model is passed through the surrogate to estimate the corresponding reflection spectra ( $S_{11}$ ), which is then compared with the target response to provide the physics based spectral consistency loss. This integration guides the diffusion model to produce metasurface geometries that are consistent with the desired EM performance.

In summary, the generation process begins from a random Gaussian noise sample which is then progressively refined through the reverse diffusion steps to obtain a metasurface geometry that satisfies the specified conditions. The integration of conditional guidance and physics-based constraints enables the model to effectively learn the mapping between EM specifications and corresponding metasurface designs for efficient inverse design.

### IV. DESCRIPTION OF DATASET & ENCODING SCHEME

To enable effective training of the diffusion-based generative model, the dataset must contain diverse geometries of meta-atoms, capable of producing varied reflection characteristics across the target frequency band of 2-18GHz. In this work, the dataset consists of 39664 samples spanning 30 distinct classes of meta-atom geometries, including both single-layer and dual-layer configurations.

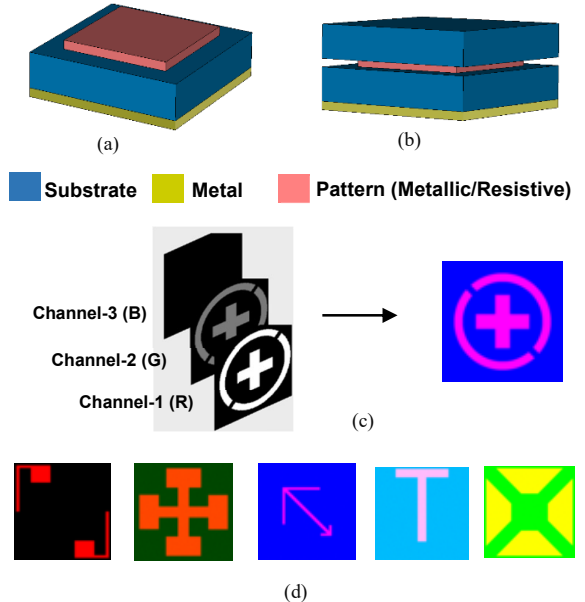


Fig. 4. Configuration of metasurface based RAS included in dataset (a) Single-layered RAS (b) Dual-layered RAS (c) Encoding scheme (d) Samples of encoded meta-atoms.

The configurations of RAS geometries included in the dataset are illustrated in Fig. 4. Dual-layer configurations are incorporated to represent practical scenarios where the

patterned layer requires protection under harsh environmental conditions. In addition to geometric diversity, each class of meta atom has been simulated using 17 commercially available substrate materials and different pattern materials (metal/resistive), enabling the dataset to account for variations in EM properties arising from material parameters. The parameter combinations for different classes have been systematically selected to generate a wide range of reflection characteristics, covering both narrowband and broadband absorption characteristics in the frequency range of 2–18 GHz. This diversity in geometry, material properties, and spectral responses is essential for enabling the diffusion model to learn a comprehensive mapping between metasurface configurations and their corresponding reflection spectra. The dataset has been generated using full-wave EM simulations in CST Studio Suite [65]. The meta-atoms have been analyzed using frequency-domain solver with periodic boundary conditions along the lateral directions, open (add space) boundaries normal to the surface, and plane-wave excitation to model the incident EM field. On generation of data, the configuration of meta atom is encoded as a 3-channel colored image. The first channel (R) represents the geometric pattern of the meta atom. Here, a pixel value of 255 indicates the presence of metallic or resistive material and 0 denotes its absence. The second channel (G) contains the same geometric pattern weighted by the normalized resistivity of the pattern material. The third channel (B) encodes the layer configuration by weighting the pattern with a binary value of 0 or 1 to represent single-layered and double-layered meta-atoms, respectively. The resulting multi-channel representation of the meta-atom is illustrated in Fig. 4c. The proposed RGB encoding scheme uniquely represents the design space, effectively reducing the extent of one-to-many mapping between EM responses and metasurface geometries. This enables more stable and physically consistent inverse design. The associated condition consists of the frequency-dependent reflection response represented by the 201-dimensional  $S_{11}$  over the frequency range of 2–18 GHz and the substrate material parameters including relative permittivity ( $\epsilon_r$ ), dielectric loss tangent ( $\tan \delta_c$ ), and substrate thickness. The material properties are incorporated as part of the input to the model, rather than being predicted at the output, to ensure that the generated designs remain physically realizable and restricted to commercially available materials.

Furthermore, to address dataset imbalance, where certain spectral characteristics dominate and bias the learning process, a thorough data analysis has been carried out. Following this, the dataset has been organized into different spectral response categories like single resonance, multiple resonance, wideband, ultra-wideband, etc. Since the number of samples across different spectral categories is varied, the dataset has been partitioned into train, validation and test sets using a stratified category-wise splitting strategy with adaptive allocation. For categories with sufficient samples an 80:10:10 split was used, whereas categories with limited samples were split using a minimum-count strategy to ensure representation in validation and test sets without exhausting the training data. This approach guarantees representation of all spectral classes during evaluation while preserving sufficient training data for rare categories. Further, during training of the model, a weighted sampling

based strategy has been employed in which each sample is assigned a weight inversely proportional to the number of data points in its corresponding spectral category. Consequently, higher sampling weights are given to underrepresented spectral categories, thereby improving the ability of the model to learn diverse spectral characteristics. This ensures uniform learning across different spectral categories and improves the robustness of the model in capturing diverse metasurface responses.

## V. RESULTS AND DISCUSSION

This section evaluates the performance of the proposed inverse design framework in terms of conditional alignment of the generated metasurface geometries. Initially, an extensive hyper parameter tuning has been performed and the following set of hyper parameters has been chosen:  $w_R=2$ ,  $w_G=1.5$ ,  $w_B=1.5$ ,  $\lambda=5$ ,  $w=5$ , initial learning rate =  $10^{-4}$  and batch size = 32. The model with the optimized set of hyper parameters has been trained for 400 epochs using Adam optimizer in conjunction with a cosine annealing learning rate schedule. Once trained, the model has been used to generate meta-atoms catering to specific conditional constraints. The data points in the test dataset have been used for this purpose. Fig. 5 illustrates the progressive evolution of the generated metasurface design from random noise to the final geometry during the iterative denoising process.

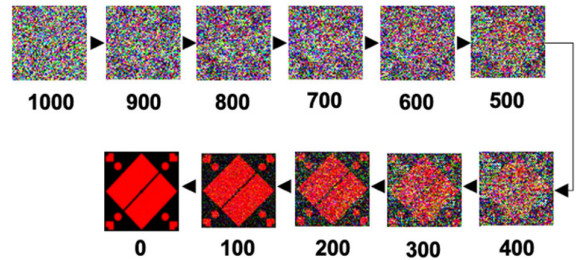


Fig. 5. Evolution of the meta-atom geometry from random noise during the iterative de-noising process at different time steps ( $t$ ).

Fig. 6 shows the comparison between the target spectra and the spectra produced on simulation of the generated meta-atoms in CST. The images of the generated meta-atom patterns are shown as inset. The comparative plots indicate that the model is capable of generating meta-atoms that can produce a variety of spectral behaviors, including narrowband, multi-resonance, and broadband reflection characteristics. From Fig. 6c, it is evident that the proposed model can even generate meta-atoms satisfying challenging constraints such as ultra-wideband characteristics (bandwidth > 10 GHz), despite the limited availability of such samples in the dataset. This capability can be attributed to the proposed weighted sampling strategy, which improves the learning of sparsely populated spectral regions during training. Further, the proposed model also demonstrated the capability to generate hybrid meta-atom geometries (Fig. 6a, Fig. 6b and Fig. 6e) by effectively combining structural features from multiple unit-cell patterns present in the training dataset, indicating strong feature-level generalization and interpolation capability. Further, the close agreement between the generated and target spectra demonstrates the effectiveness of the FiLM-based conditioning mechanism.

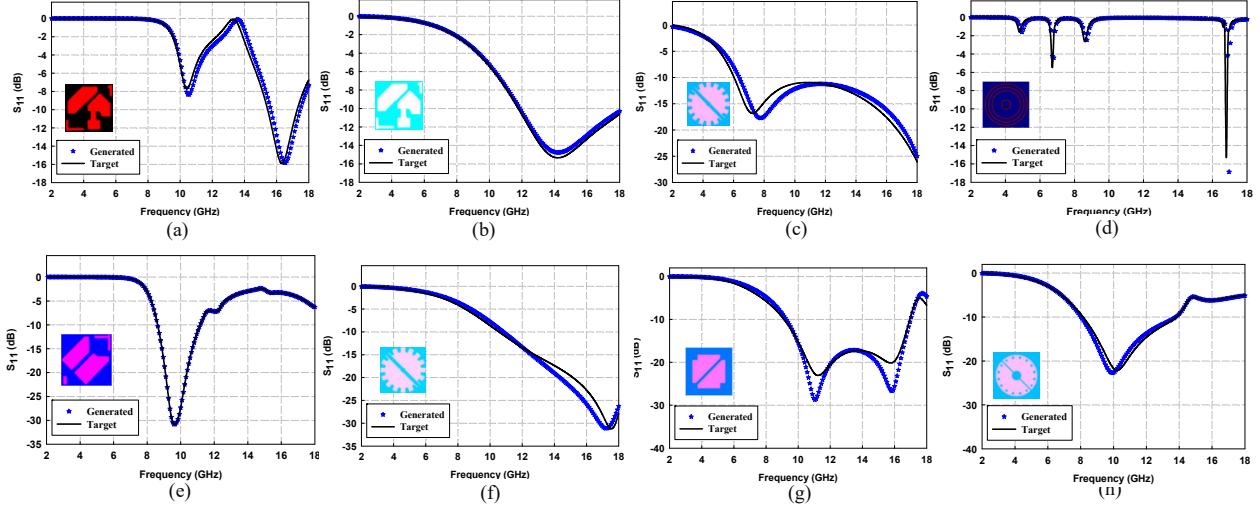


Fig. 6. Comparison between target spectra and the spectra obtained on simulation of generated meta-atoms for different samples in the test set. (a) Sample-1 (Material: RT/Duroid 5880 ( $\epsilon_r=2.2$ ,  $\tan\delta=0.0009$ ,  $t=1.575\text{mm}$ ); Single-layered; Metallic pattern) (b) Sample-2 (Material: RO4835 ( $\epsilon_r=3.48$ ,  $\tan\delta=0.0037$ ,  $t=1.524\text{mm}$ ); Double-layered; Resistive pattern (100 ohm/sq.)) (c) Sample-3 (Material: AD255C ( $\epsilon_r=2.6$ ,  $\tan\delta=0.0013$ ,  $t=3.175\text{mm}$ ); Double-layered; Resistive pattern (70 ohm/sq.)) (d) Sample-4 (Material: RO4835 ( $\epsilon_r=3.48$ ,  $\tan\delta=0.0037$ ,  $t=1.524\text{mm}$ ); Double-layered; Metallic pattern) (e) Sample-5 (Material: RO4835 ( $\epsilon_r=3.48$ ,  $\tan\delta=0.0037$ ,  $t=1.524\text{mm}$ ); Double-layered; Metallic pattern) (f) Sample-6 (Material: RO4533 ( $\epsilon_r=3.45$ ,  $\tan\delta=0.0025$ ,  $t=1.524\text{mm}$ ); Double-layered; Resistive pattern (75 ohm/sq.)) (g) Sample-7 (Material: Kappa 438 ( $\epsilon_r=4.38$ ,  $\tan\delta=0.005$ ,  $t=1.524\text{mm}$ ); Double-layered; Resistive pattern (50 ohm/sq.)) (h) Sample-8 (Material: RO4360G2 ( $\epsilon_r=6.4$ ,  $\tan\delta=0.0038$ ,  $t=1.524\text{mm}$ ); Double-layered; Resistive pattern (75ohm/sq)).

The generated designs also exhibit well-defined structural features that closely resemble realistic meta-atoms, with feature dimensions remaining within practical fabrication limits. This demonstrates the effectiveness of the dataset, which was constructed while incorporating fabrication constraints to ensure the generation of physically realizable metasurface geometries.

In addition, the ability of the model to produce multiple geometrically distinct solutions corresponding to the same spectral requirement is shown in Fig. 7.

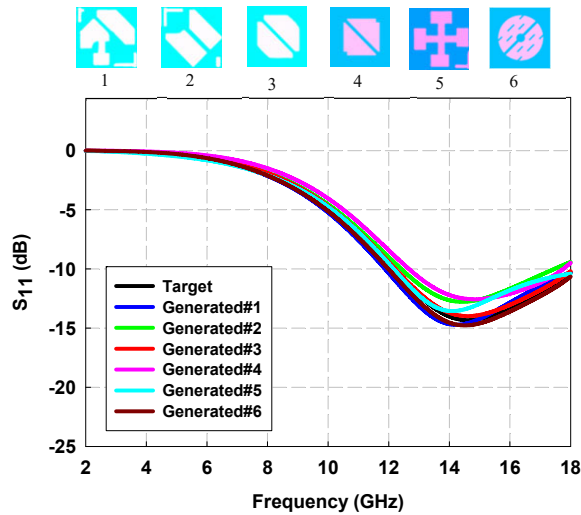


Fig. 7. Diverse metasurface geometries generated by the proposed model for the same target reflection characteristics.

The diversity of the generated meta-atom geometries has been quantified using the following average pairwise structural dissimilarity metric ( $D$ ):

$$D = \frac{2}{N(N-1)} \sum_{i<j} [\lambda d_1 + (1-\lambda)d_2] \quad (12)$$

$$\text{Where, } d_1 = 1 - \frac{|M_i \cap M_j|}{|M_i \cup M_j| + \epsilon}; \quad d_2 = 1 - \frac{|R_i^{(\delta)} \cap R_j^{(\delta)}|}{|R_i^{(\delta)} \cup R_j^{(\delta)}| + \epsilon}$$

$M_i$  and  $M_j$  denote the binary masks corresponding to the  $i^{\text{th}}$  and  $j^{\text{th}}$  generated meta-atom geometries, respectively, where 1 represents the presence of pattern material and 0 represents the absence of it.  $d_1$  measures the variations in pattern material distribution between a pair of images using the intersection over union (IoU) distance between binary masks.  $R_i^{(\delta)}$  and  $R_j^{(\delta)}$  denote the boundary regions of the corresponding masks, obtained by selecting pixels lying within a distance  $\delta$  from the metal edges.  $d_2$  quantifies fine-scale geometric differences by comparing the contour regions. The weighting factor  $\lambda$  controls the relative contribution of global structural variation and local boundary variation. A small constant  $\epsilon$  is introduced in the denominator to ensure numerical stability.  $N$  denotes the number of generated images. The diversity metric yielded a high score of 0.803 for the proposed model. Further, the generated samples exhibited high spectral consistency with a very low average mean squared error of 0.001 under identical conditioning. This indicates the capability of the diffusion framework to explore diverse design possibilities within the solution space. Such diversity is particularly beneficial as it provides designers with multiple candidate geometries allowing flexibility in fabrication and implementation.

## VI. ABLATION ANALYSIS

This section presents an ablation analysis to assess the effectiveness of diffusion-based models for inverse design of metasurface-based RAS relative to other generative frameworks such as conditional WGAN-GP and VAE,

along with a systematic assessment of different conditioning mechanisms. The performance of each variant is evaluated using multiple metrics including average spectral mean squared error (MSE), accumulated average error (AAE), average band alignment accuracy (BAA), and the percentage of valid designs. All evaluation metrics are computed over the test dataset. The average spectral MSE and AAE quantify pointwise agreement between the target and generated spectra. They are defined as:

$$MSE = \frac{1}{N_{test}} \sum_{j=1}^{N_{test}} \frac{1}{N_f} \sum_{i=1}^{N_f} \left( |S_{11(gen)}(f_i)| - |S_{11(target)}(f_i)| \right)^2 \quad (13)$$

$$AAE = \frac{1}{N_{test}} \sum_{j=1}^{N_{test}} \frac{1}{N_f} \sum_{i=1}^{N_f} \left| |S_{11(gen)}(f_i)| - |S_{11(target)}(f_i)| \right| \quad (14)$$

Where  $|S_{11(gen)}(f_i)|$  and  $|S_{11(target)}(f_i)|$  denote the generated and target spectral response at the  $i^{\text{th}}$  frequency point ( $f_i$ ).  $N_f$  denotes total number of frequency points and  $N_{test}$  denote number of data points in the test data set.

BAA measures the overlap between the desired and generated absorption regions and is defined as,

$$BAA = \frac{1}{N_{test}} \sum_{j=1}^{N_{test}} \frac{|B_{target}(j) \cap B_{gen}(j)|^2}{|B_{target}(j)|} \quad (15)$$

where  $B_{target}$  and  $B_{gen}$  refer to the set of frequency points in the target spectrum and generated spectrum respectively where  $|S_{11}| \leq -10\text{dB}$ . The percentage of valid designs denote the fraction of generated designs that has a band alignment greater than 0.8. Table I presents the summary of the ablation analysis *w.r.t.* the above-mentioned evaluation metrics. It is clear from Table I that the baseline diffusion model is better compared to conditional WGAN-GP *w.r.t.* different metrics. The geometries generated by VAE exhibited poor structural quality, characterized by numerous irregular fine-scale features that were difficult to simulate in CST and impractical for fabrication. Hence, the corresponding metrics are not included. Further, it is evident that the progressive inclusion of conditioning mechanisms leads to consistent improvement across all performance metrics. In particular, the integration of the surrogate model and FiLM-based conditioning significantly enhances spectral accuracy and band alignment. Overall, these results underscore the importance of combining physics-guided learning with feature-wise conditioning for robust inverse metasurface design.

**Table I** Summary of ablation analysis

Model	Avg. MSE	AAE	BAA	Valid designs
WGAN-GP	0.049	0.168	0.302	30%
Baseline diffusion	0.045	0.140	0.483	40%
Baseline diffusion with SES and condition concatenated with image at input	0.042	0.132	0.578	60%
Baseline diffusion with SES and condition injection via FiLM in U-Net (Proposed)	0.0006	0.016	0.958	100%

In addition, it is to be noted that the proposed model generates the suitable design for meta-atom in approximately 30 seconds for a given target response, whereas conventional design approaches based on iterative

full-wave simulations may require several months under comparable computational resources.

## VII. EXPERIMENTAL VALIDATION

This section presents the practical feasibility of the proposed inverse design framework via experimental validation. The proposed model has been used to predict the meta-atom geometry for a specific reflection spectrum as shown in Fig. 8a to be realized using RO4835 substrate material ( $\epsilon_r=3.48$ ,  $\tan\delta=0.0037$ ,  $t=1.524\text{mm}$ ). The generated meta-atom (Fig. 8b) has been used to configure a  $15\text{cm} \times 15\text{cm}$  planar RAS in CST Studio suite as shown in Fig. 8c and Fig. 8d. The planar RAS has been checked for fabrication feasibility by confirming that the minimum feature size is greater than  $0.1\text{mm}$ . Once confirmed via simulation, the same planar RAS has been fabricated via laser etching procedure.

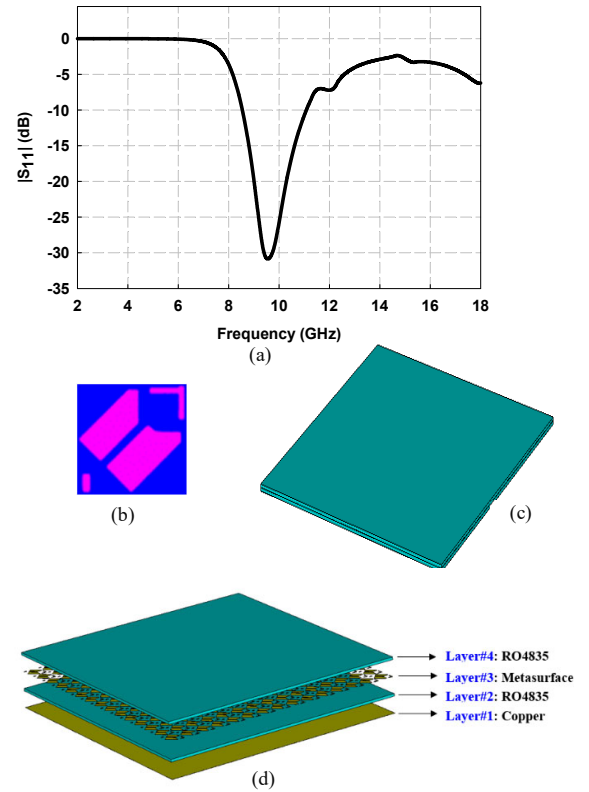


Fig. 8. (a) Target reflection spectra (b) Meta atom geometry generated using the proposed inverse design framework (c) Simulated model of planar RAS ( $15\text{cm} \times 15\text{cm}$ ) (d) Exploded side view of simulated planar RAS.

The fabricated prototype is shown in Fig. 9. Since the target spectra has  $S_{11} \leq -10\text{dB}$  within the frequency range of 8.5 GHz to 11 GHz, the reflection characteristics ( $S_{11}$ ) of the fabricated planar RAS under normal incidence in this frequency range has been measured using a free-space measurement setup consisting of an Agilent Technologies PNA Network Analyzer (N5227A) and a pair of X-band horn antennas. The measurement set-up is shown in Fig. 10a. The absorption performance of the structure has been then evaluated based on the following relation:

$$|A|^2 = 1 - |S_{11}|^2 - |S_{21}|^2 \quad (16)$$

where  $|A|^2$ ,  $|S_{11}|^2$  and  $|S_{21}|^2$  denote the absorbed, reflected, and transmitted power, respectively. In the present configuration, the transmission term  $|S_{21}|^2$  is negligible due to the presence of the continuous metallic backing, resulting in  $|A|^2 \approx 1 - |S_{11}|^2$ .

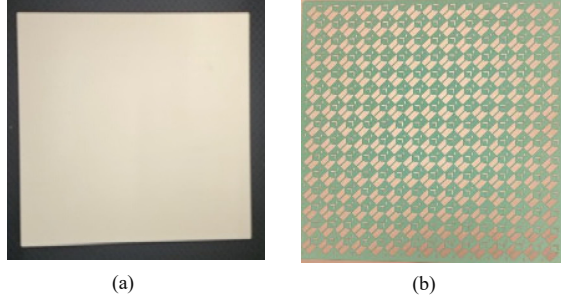


Fig. 9. Fabricated prototype of planar RAS (15cm x 15cm) (a) Top view (b) Etched metasurface pattern (green color denote the photoresist layer).

The frequency-dependent absorption characteristics obtained from measurements have been compared with the generated results and the target spectrum in Fig. 10b. It can be observed that the fabricated RAS achieves greater than 90% power absorption within the targeted frequency range. Minor deviations can be attributed to fabrication tolerances and measurement uncertainties. This agreement confirms the capability of the proposed framework to accurately translate the desired EM response into a realizable metasurface design. Table II presents the comparison of existing generative techniques and the proposed approach *w.r.t.* inverse design of metasurfaces.

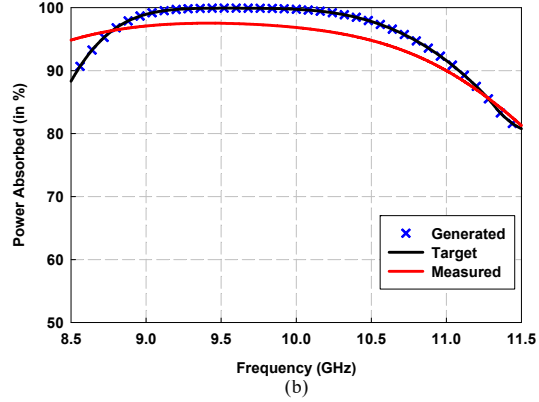


Fig. 10. (a) Experimental set up for measurement of  $S_{11}$  (b) Target, generated and measured absorption characteristics of RAS.

**Table II** Comparison of proposed approach with prior art

Ref.	Freq. range	Model	Size of dataset	Condition	Physics Integration	Conditioning Quality Assessment			Diversity	Exp. validation
						Qualitative	Quantitative	Scenarios		
[40]	170 THz-600 THz	GAN	8000	Transmission spectra	Yes	Yes	No	Limited	No	No
[41]	8 GHz - 12 GHz	GAN	54000	Scattering parameters	No	Yes	No	Limited	No	No
[42]	7 GHz - 20 GHz	GAN	4700	Axial ratio	No	Yes	No	Limited	No	Yes
[43]	4 GHz - 20 GHz	GAN	850	Reflection spectra	No	Yes	No	One	No	No
[44]	25 THz - 75 THz	GAN	18768	Absorption spectra	Yes	Yes	Yes	Limited	Yes	No
[47]	20 GHz - 30 GHz	GAN	12700	Reflection spectra	Yes	Yes	Yes	Limited	No	No
[48]	8 GHz - 12 GHz	GAN	24000	Transmission spectra	Yes	Yes	Yes	Limited	Yes	No
[50]	15 GHz - 31 GHz	VAE	19854	Transmission spectra	Yes	Yes	No	One	No	No
[51]	15 GHz - 31 GHz	VAE	34000	Transmission spectra	Yes	Yes	No	Limited	No	No
[52]	5 GHz - 15 GHz	VAE	3000	Reflection spectra	No	Yes	Yes	Limited	No	No
[53]	1 GHz - 18 GHz	VAE	3116	Scattering parameters	Yes	Yes	No	Limited	No	Yes
[54]	2 GHz - 22 GHz	VAE	13401	Absorption spectra	No	Yes	No	Limited	No	Yes
[55]	2 GHz - 40 GHz	VAE	26000	Scattering parameters	Yes	Yes	No	Limited	No	Yes
<b>Present work</b>	<b>2 GHz - 18GHz</b>	<b>Diffusion</b>	<b>39664</b>	<b>Reflection spectra</b>	<b>Yes</b>	<b>Yes</b>	<b>Yes</b>	<b>Wide</b>	<b>Yes</b>	<b>Yes</b>

## VIII. CONCLUSION

This paper presented a FiLM-conditioned diffusion framework for the inverse design of metasurface-based RAS, incorporating a pretrained surrogate model for physics-aware regularization. The proposed approach effectively learns the mapping between target reflection spectra and metasurface geometries, achieving high conditional fidelity, low spectral MSE, and strong band alignment accuracy, while maintaining the ability to generate diverse design solutions. The ablation study demonstrates the role of FiLM conditioning and surrogate-based constraints in improving condition alignment. Furthermore, experimental validation through fabrication and measurement shows good agreement between measured, simulated, and target responses, confirming the practical realizability and effectiveness of the proposed method. Further, the proposed model generates the suitable design for meta-atom in approximately 30 seconds for a given target response, whereas conventional design approaches based on iterative full-wave simulations may require several months under comparable computational resources. Overall, the proposed framework provides an efficient and scalable solution for metasurface inverse design, significantly reducing the reliance on computationally expensive EM simulations. As future work, the approach can be extended to incorporate oblique angles of incidence and polarization dependent responses thereby further enhancing its applicability to real-world EM design problems.

## ACKNOWLEDGMENT

We express our gratitude to Council of Scientific and Industrial Research (CSIR), India for supporting this research activity. We also express our gratitude to CSIR-4PI for providing access to HPC facility, the Department of Electronics, Cochin University of Science and Technology (CUSAT) for supporting S-parameter measurements.

## DATA AVAILABILITY STATEMENT

The dataset supporting this study is not publicly available due to confidentiality restrictions associated with sponsored research projects involving proprietary metasurface designs.

## CONFLICT OF INTEREST

The authors declare that they have no conflict of interest.

## REFERENCES

- [1] C. L. Holloway, E. F. Kuester, J. A. Gordon, J. O. Hara, J. Booth, and D. R. Smith, "An overview of the theory and applications of metasurfaces: The two-dimensional equivalents of metamaterials," *IEEE Antennas and Propagation Magazine*, vol. 54, no. 2, pp. 10–35, Apr. 2012.
- [2] N. Yu, P. Genevet, M. A. Kats, F. Aieta, J. Tetienne, F. Capasso, and Z. Gaburro, "Light propagation with phase discontinuities: Generalized laws of reflection and refraction," *Science*, vol. 334, no. 6054, pp. 333–337, Oct. 2011.
- [3] N. Yu and F. Capasso, "Flat optics with designer metasurfaces," *Nature Materials*, vol. 13, no. 2, pp. 139–150, Feb. 2014.
- [4] V. Joy, A. Dileep, P. V. Abhilash, R. U. Nair, H. Singh, "Metasurfaces for stealth applications: A comprehensive review," *Journal of Electronics Materials*, vol. 50, no. 6, pp. 3129–3148, Jun. 2021.
- [5] H. Hao, S. Du, and T. Zhang, "Small-Size Broadband Coding Metasurface for RCS Reduction Based on Particle Swarm Optimization Algorithm," *Progress in Electromagnetics Research M*, vol. 81, pp. 97–105, 2019.
- [6] J. Hou, H. Lin, W. Xu, X. Shi, R. Tang, L. Chen, and Y. Tian, "Customized inverse design of metamaterial absorber based on target-driven deep learning method," *IEEE Access*, vol. 8, pp. 211849–211859, 2020.
- [7] X. Ni, Z. J. Wong, M. Mrejen, Y. Wang, and X. Zhang, "An ultrathin invisibility skin cloak for visible light," *Science*, vol. 349, no. 6254, pp. 1310–1314, Sep. 2015.
- [8] Y. Yang, W. Li, K. N. Salama, and A. Shamim, "Polarization-insensitive and transparent frequency-selective surface for dual-band GSM shielding," *IEEE Transactions on Antennas and Propagation*, vol. 69, no. 5, pp. 2779–2789, May 2021.
- [9] X. Ni, A. Kildishev, and V. Shalaev, "Metasurface holograms for visible light," *Nature Comm.* vol. 4, Art. no. 2807, Nov. 2013.
- [10] Y. Hu, X. Luo, Y. Chen, Q. Liu, X. Liu, Y. Wang, N. Liu and H. Duan, "3D-integrated metasurfaces for full-colour holography," *Light: Science and Applications*, vol. 8, Art. no. 86, Sep. 2019.
- [11] M. Selvaraj, R. Vijay, and R. Anbazhagan, "Reflective metasurface for 5G and beyond wireless communications," *Scientific Reports*, vol. 15, Art. no. 126, 2025.
- [12] Q. Xiong, Z. Zhang, C. Huang, M. Pu, J. Luo, Y. Guo, J. Ye, W. Pan, X. Ma, L. Yan, and X. Luo, "Amplitude–phase independently encoding space-division multiplexed wireless communication using beamforming reconfigurable metasurfaces," *Advanced Optical Materials*, vol. 12, no. 28, 2024.
- [13] W. T. Chen, A. Y. Zhu, V. Sanjeev, M. Khorasaninejad, Z. Shi, E. Lee, and F. Capasso, "A broadband achromatic metalens for focusing and imaging in the visible," *Nature Nanotechnology*, vol. 13, no. 3, pp. 220–226, Mar. 2018.
- [14] Q. He, S. Sun, S. Xiao, and L. Zhou, "High-efficiency metasurfaces: Principles, realizations, and applications," *Advanced Optical Materials*, vol. 6, no. 19, Art. no. 1800415, 2018.
- [15] S. Chen, W. Liu, Z. Li, H. Cheng, and J. Tian, "Metasurface-empowered optical multiplexing and multifunction," *Advanced Materials*, vol. 32, no. 3, Art. no. 1805912, 2020.
- [16] M. Khorasaninejad and F. Capasso, "Broadband multifunctional efficient meta-gratings based on dielectric waveguide phase shifters," *Nano Letters*, vol. 15, no. 10, pp. 6709–6715, Oct. 2015.
- [17] O. Bouvard, M. Lanini, and L. Burnier, "Structured transparent low-emissivity coatings with high microwave transmission," *Applied Physics A*, vol. 123, no. 1, Art. no. 66, 2017.
- [18] S. Dong, G. Hu, Q. Wang, Y. Jia, Q. Zhang, G. Cao, J. Wang, S. Chen, D. Fan, W. Jiang, Y. Li, A. Alu, and C.-W. Qiu, "Loss-assisted metasurface at an exceptional point," *ACS Photonics*, vol. 7, no. 12, pp. 3321–3327, Dec. 2020.
- [19] J. Fleury, M. Lanini, and C. Pose, "Wide band-pass frequency selective surface with reduced periodicity for energy-efficient windows at higher frequencies," *Applied Physics A*, vol. 126, no. 6, Art. no. 417, 2020.
- [20] S. D. Campbell, D. Sell, R.P. Jenkins, E. B. Whiting, J. A. Fan and D.H. Werner, "Review of numerical optimization techniques for meta-device design," *Optical Materials Express*, vol. 9, no. 4, pp. 1842–1863, 2019.
- [21] J. S. Jensen and O. Sigmund, "Topology optimization for nanophotonics," *Laser & Photonics Reviews*, vol. 5, no. 2, pp. 308–321, Mar. 2011.
- [22] W. Li, F. Meng, Y. Chen, Y. Li, and X. Huang, "Topology optimization of photonic and phononic crystals and metamaterials: A review," *Advanced Theory and Simulations*, vol. 2, Art. no. 1900017, 2019.
- [23] J. A. Bossard, L. Lin, S. Yun, L. Liu, D. H. Werner, and T. S. Mayer, "Near-ideal optical metamaterial absorbers with super-octave bandwidth," *ACS Nano*, vol. 8, no. 2, pp. 1517–1524, Feb. 2014.
- [24] S. Jafar-Zanjani, S. Inampudi, and H. Mosallaei, "Adaptive genetic algorithm for optical metasurfaces design," *Scientific Reports*, vol. 8, no. 1, Art. no. 11040, 2018.
- [25] S. Chakravarty, R. Mittra, and N. R. Williams, "Application of a microgenetic algorithm (MGA) to the design of broadband microwave absorbers using multiple frequency selective surface screens buried in dielectrics," *IEEE Transactions on Antennas and Propagation*, vol. 50, no. 3, pp. 284–296, Mar. 2002.

- [26] M. A. Gingrich and D. H. Werner, "Synthesis of low/zero index of refraction metamaterials from frequency selective surfaces using genetic algorithms," *Electronics Letters*, vol. 41, no. 23, pp. 1266–1267, Nov. 2005.
- [27] A. Lewis, G. Weis, M. Randall, A. Galehdar and D. Thiel, "Optimising efficiency and gain of small meander line RFID antennas using ant colony system," in *Proceedings of the IEEE Congress on Evolutionary Computation*, Norway, 2009, pp. 1486–1492.
- [28] D. Z. Zhu, P. L. Werner, and D. H. Werner, "Design and optimization of 3-D frequency-selective surfaces based on a multiobjective lazy ant colony optimization algorithm," *IEEE Transactions on Antennas and Propagation*, vol. 65, no. 12, pp. 7137–7149, Dec. 2017.
- [29] D. Z. Zhu, M. D. Gregory, P. L. Werner, and D. H. Werner, "Fabrication and characterization of multiband polarization-independent 3-D printed frequency selective structures with ultra-wide fields of view," *IEEE Transactions on Antennas and Propagation*, vol. 66, no. 11, pp. 6096–6105, Nov. 2018.
- [30] J. Robinson and Y. Rahmat-Samii, "Particle swarm optimization in electromagnetics," *IEEE Transactions on Antennas and Propagation*, vol. 52, no. 2, pp. 397–407, Feb. 2004.
- [31] A. V. Kildishev, U. K. Chettiar, Z. Liu, V. M. Shalaev, D.-H. Kwon, Z. Bayraktar, and D. H. Werner, "Stochastic optimization of low-loss optical negative-index metamaterial," *Journal of the Optical Society of America B*, vol. 24, no. 10, pp. A34–A39, Oct. 2007.
- [32] S. So, T. Badloe, J. Noh, J. Bravo-Abad, and J. Rho, "Deep learning enabled inverse design in nanophotonics," *Nanophotonics*, vol. 9, no. 5, pp. 1041–1057, 2020.
- [33] W. Ma, Z. Liu, Z. A. Kudyshev, A. Boltasseva, W. Cai, and Y. Liu, "Deep learning for the design of photonic structures," *Nature Photonics*, vol. 15, pp. 77–90, Jan. 2021.
- [34] J. Peurifoy, Y. Shen, L. Jing, Y. Yang, F. Cano-Renteria, B. Delacy, J. D. Joannopoulos, M. Tegmark, and M. Soljačić, "Nanophotonic particle simulation and inverse design using artificial neural networks," *Science Advances*, vol. 4, Art. no. eaar4206, 2018.
- [35] S. So, J. Mun, and J. Rho, "Simultaneous inverse design of materials and structures via deep learning: Demonstration of dipole resonance engineering using core-shell nanoparticles," *ACS Applied Materials & Interfaces*, vol. 11, no. 27, pp. 24264–24268, 2019.
- [36] I. Malkiel, M. Mrejen, A. Nagler, U. Arieli, L. Wolf, and H. Suchowski, "Plasmonic nanostructure design and characterization via deep learning," *Light: Science and Applications*, vol. 7, . 60, 2018.
- [37] D. Liu, Y. Tan, E. Khoram, and Z. Yu, "Training deep neural networks for the inverse design of nanophotonic structures," *ACS Photonics*, vol. 5, no. 4, pp. 1365–1369, 2018.
- [38] X. He, X. Cui, and C. T. Chan, "Constrained tandem neural network assisted inverse design of metasurfaces for microwave absorption," *Optics Express*, vol. 31, no. 25, pp. 40969–40979, 2023.
- [39] Z. Hu, W. Su, K. Hu, and B. Tang, "A deep learning-driven forward and inverse cooperative network for circular dichroism in chiral metasurfaces," *Journal of Materials Chemistry C*, vol. 13, pp. 9717–9723, 2025.
- [40] Z. Liu, D. Zhu, K. Lee, A. S. Kim, and J. R. W. Mark, "Generative model for the inverse design of metasurfaces," *ACS Nano*, vol. 12, no. 7, pp. 7073–7083, 2018.
- [41] M. Kiani and J. Kiani, "Conditional generative adversarial networks for inverse design of multifunctional microwave metasurfaces," *Advanced Photonics Research*, vol. 3, Art. no. 202200110, 2022.
- [42] P. Naseri, G. Goussetis, N. J. G. Fonseca, and S. V. Hum, "Synthesis of multi-band reflective polarizing metasurfaces using a generative adversarial network," *Scientific Reports*, vol. 12, 17006, 2022.
- [43] A. Nezaratzadeh, S. M. Hashemi, and M. Bod., "Prediction of multi-layer metasurface design using conditional deep convolutional generative adversarial networks," *International Journal for Light and Electron Optics*, vol. 313, p. 172005, 2024.
- [44] Y. Zeng, H. Cao, and X. Jin, "Anchor-controlled generative adversarial network for high-fidelity electromagnetic and structurally diverse metasurface design," arXiv preprint arXiv:2408.16231v2, 2024.
- [45] A. Mall, A. Patil, A. Sethi & A. Kumar, "A cyclical deep learning based framework for simultaneous inverse and forward design of nanophotonic metasurfaces," *Scientific Reports*, Article number: 19427, 2020.
- [46] C. Liu, W. M. Yu, Q. Ma, L. Li, and T. J. Cui, "Intelligent coding metasurface holograms by physics-assisted unsupervised generative adversarial network," *Photonics Research*, vol. 9, no. 4, pp. B159–B167, Apr. 2021.
- [47] G. Dai, H. Li, X. Zhang, and Y. Liu, "Single-layer metasurface design with symmetrical free-form patterns using generative adversarial networks," *Applied Soft Computing*, vol. 127, Art. no. 109353, 2022.
- [48] H. P. Wang, D. M. Cao, X. Y. Pang, X. H. Zhang, S. Y. Wang, W. Y. Hou, C. C. Nie, and Y. B. Li, "Inverse design of metasurfaces with customized transmission characteristics of frequency band based on generative adversarial networks," *Optics Express*, vol. 31, no. 23, pp. 37763–37783, 2023.
- [49] A. Mall, A. Patil, D. Tamboli, A. Sethi and A. Kumar, "Fast design of plasmonic metasurfaces enabled by deep learning," *Journal of Physics D: Applied Physics*, vol. 53, no. 49, October 2020.
- [50] P. Naseri and S. V. Hum, "A Machine learning-based approach to synthesize multilayer metasurfaces," *2020 IEEE International Symposium on Antennas and Propagation and North American Radio Science Meeting*, Montreal, QC, Canada, 2020, pp. 933-934.
- [51] P. Naseri and S. V. Hum, "A generative machine learning-based approach for inverse design of multilayer metasurfaces," *IEEE Transactions on Antennas and Propagation*, vol. 69, no. 9, pp. 5725–5739, Sep. 2021.
- [52] J. -H. Kim and I. -P. Hong, "An Optimization Approach Based on Separated Latent Space for Inverse Design of Metasurfaces," in *IEEE Antennas and Wireless Propagation Letters*, vol. 23, no. 7, pp. 2135–2139, July 2024.
- [53] W. Ding, J. Chen, and R.-X. Wu, "A generative meta-atom model for metasurface-based absorber designs," *Advanced Optical Materials*, vol. 11, no. 2, Art. no. 2201959, 2022.
- [54] Q. Li, J. Wang, T. Lei, T. Xiang, C. Qin and M. Yang, "Design of Metamaterials for Absorbers Based on Variational Autoencoder," *IEEE Access*, vol. 12, pp. 92328–92336, 2024.
- [55] H.-I. On, L. Jeong, T.-M. Seo, Y. Jo, W. Choi, D.-J. Kang, J.-H. Park, and H.-J. Lee, "Novel method of performance-optimized metastructure design for electromagnetic wave absorption in specific band using deep learning," *Engineering Applications of Artificial Intelligence*, vol. 137, p. 109274, 2024.
- [56] P. Pillai, B. RaI, and P. Pal, "Modified variational autoencoder for inversely predicting plasmonic nanostructures for generating structural color," *Scientific Reports*, vol. 13, Art. no. 3536, 2023.
- [57] S. Warrior, J. Dontabhaktuni, "Hybrid quantum generative adversarial networks to inverse design metasurfaces for incident angle-independent unidirectional transmission," arXiv preprint arXiv:2507.03518, 2025.
- [58] X. Ding, Y. Wang, Z. Xu, W. J. Welch, and Z. J. Wang, "Continuous conditional generative adversarial networks: Novel empirical losses and label input mechanisms," *IEEE Trans. Pattern Analysis and Machine Intelligence*, vol. 45, no. 7, pp. 8143–8158, Jul. 2023.
- [59] W. Chen and F. Ahmed, "PaDGAN: A generative adversarial network for performance augmented diverse designs," arXiv preprint arXiv:2002.11304, 2020.
- [60] C. Saharia, J. Ho, W. Chan, T. Salimans, D. J. Fleet and M. Norouzi, "Image super-resolution via iterative refinement," *IEEE Transactions on Pattern Analysis and Machine Intelligence*, vol. 45, no. 4, pp. 4713–4726, April 2023.
- [61] X. Zheng, J. Shiomi and T. Yamada, "Optimizing metamaterial inverse design with 3D conditional diffusion model and data augmentation," *Advanced Materials Tech.*, vol. 10, 10p., 2025.
- [62] J. Ho, A. Jain, and P. Abbeel, "Denoising diffusion probabilistic models," in *Proceedings of the 34th International Conference on Neural Information Processing Systems (NeurIPS)*, Vancouver, BC, Canada, 2020, pp. 6840–6851.
- [63] J. Ho and T. Salimans, "Classifier-free diffusion guidance," *arXiv preprint arXiv:2207.12598*, 2022.
- [64] E. Perez, F. Strub, H. de Vries, V. Dumoulin, and A. Courville, "FiLM: Visual reasoning with a general conditioning layer," in *Proceedings of the Thirty-Second AAAI Conference on Artificial Intelligence*, Article No.: 483, pp. 3942 - 3951, 2018.
- [65] CST Studio Suite®, CST AG, Germany, www.cst.com